Acoustic and exact elastic impedance variations during CO₂ injection at the CaMI.FRS

Yichuan Wang and Don Lawton

ABSTRACT

For seismic monitoring injected CO_2 during geologic CO_2 storage, it is useful to measure time-lapse (TL) variations of seismic impedance. Acoustic impedance (AI) and elastic impedance (EI) give direct connections to the mechanical and fluid-related properties of the CO_2 storage complex. However, evaluation of their subtle TL variations is complicated by the scaling and low-frequency uncertainties, and the various EI definitions involve different approximations and do not represent an elastic property of the medium. To solve these issues, we perform accurate waveform calibration for TL seismic data, and apply a robust impedance-inversion approach based on calibration of seismic records by using the well-log data. We also use an exact expression of EI in a matrix form, which truly represents the intrinsic physical property and accurately describes P- and S-wave propagations at arbitrary incidence angles. The above approaches are applied to TL DAS VSP data from the Field Research Station CO_2 injection project in southern Alberta, Canada. High-quality baseline, monitor and TL impedance-difference images are obtained. TL impedance variations are observed within the CO_2 injection zone, which are interpreted as being related to the CO_2 injection. AI and EI measured from this approach can be advantageous tools for monitoring the distribution and migration of CO_2 plumes within the CO_2 storage complex.

INTRODUCTION

Carbon storage in subsurface geologic formation is a promising technology for reducing CO_2 emissions. Different types of geophysical (e.g., seismic, geoelectric, electromagnetic, gravity) methods are used to monitor the distribution of CO_2 plumes within the injection zone. Time-lapse (TL) seismic methods (e.g., Lumley, 2001), including vertical seismic profiles (VSPs), have the advantage of providing a spatially continuous and high-resolution assessment of physical property changes within the CO_2 storage complex. In addition, the rapid development of distributed acoustic sensing (DAS) technology promotes its use in borehole VSP for TL monitoring, with the advantages such as long-term deployment, low installation cost, large vertical coverage at small spatial sampling, and concurrent data acquisition and CO_2 injection. To quantitatively correlate seismic data to geologic and well-log observations, it is useful to transform them into various kinds of lithologic or petrophysical attributes, such as acoustic and elastic impedances. Estimating impedance variations by using DAS VSP data for monitoring injected CO_2 in subsurface is presented in this report.

Impedance is a key material property characterizing reflection and transmission of seismic waves across boundaries (Aki and Richards, 2002). For P-wave at normal incidence, the acoustic impedance (AI) is the product of density ρ and P-wave velocity V_P:

$$AI = \rho V_{\mathrm{P}}. \tag{1}$$

Different extensions of this AI to arbitrary oblique incidence are then known as the elastic impedance (EI). For a series of layers, the impedance Z of kth layer can be inverted from seismic reflectivity series as (e.g., Lindseth, 1979)

$$Z_k = Z_{0k} \prod_{i=0}^{k-1} \frac{1+R_i}{1-R_i} \approx Z_{0k} \exp\left(2\sum_{i=0}^{k-1} R_i \right), \qquad (2)$$

where R_i denotes the reflectivity of the boundary between layer i and layer $i+1$, and Z_{0k} denotes a slowly varying function containing an arbitrary scalar and some additional low-frequency "drift". This drift can be caused by the discretization, noise, and various types of errors in R_i accumulated by the integration (Wang and Morozov, 2020). In this report, these uncertainties described by Z_{0k} are removed by using additional well-log data through the well-log-based calibration (Morozov and Ma, 2009), which is straightforward and does not require sophisticated inverse algorithm.

The various EIs constructed by the integration of reflectivity series in equation 2 involve different approximations and do not represent an intrinsic elastic property of the medium. Instead of inaccurately taking EI as a single scalar, it is important to measure it in a rigorous form that characterizes P- and SV- reflection and conversion simultaneously. In this report, we measure such exact EI in a matrix form proposed by Morozov (2010), which can represent a mechanical property of the medium and lead to reflection/conversion equations at all incidence angles without any approximation. We derive the variations of AI and matrix EI from reflection signal of DAS VSP data acquired at the Field Research Station (FRS) in Alberta, Canada, developed by the Containment and Monitoring Institute (CaMI). TL interpretations of these measured results help in characterizing the distribution and migration of injected CO_2 at the CaMI FRS.

Data and geology of the CaMI FRS

The CaMI FRS is in Newell County, southern Alberta, Canada. At the FRS, there is one CO_2 injection well and two observation wells (OBS1 and OBS2, Figure 1). DAS fiber cables are from the top to the maximum depth of 348 m in OBS1 and 334 m in OBS2. Several DAS VSP surveys have been acquired at the FRS, and the surveys analyzed in this report include the baseline one acquired in May 2017 and the monitor one acquired in March 2021. Since the first CO_2 injection in August 2017, there had been approximately 34 tonnes of CO_2 injected at the FRS prior to the acquisition date of March 2021. Figure 1 shows the shot locations of one walk-around and three walk-away lines of the monitor survey. This study measures the impedance variations for walk-away VSP data acquired along Line 13. The seismic acquisition repeatability for Line 13 is good due to the permanent installation of DAS fiber cables and the same source type.

The FRS is within the area of the Interior Platform Structural Province of the Western Canada Sedimentary Basin, which contains interbedded sandstone and shale-dominated strata (~1000 m thick) of Cretaceous age and overlying Quaternary glacial tills and soils (~30 m thick). The Basal Belly River Sandstone (BBRS) is the target formation for CO_2 injection at the FRS. This formation is composed of fine to medium-grained and poorly-to-well-sorted sandstone with the thickness of 7 m (~295 to 302 m in depth), the permeability of approximately 0.4–1.2 mD, and the average porosity of approximately

11%. The BBRS injection zone is sealed above by the Foremost Formation which is 152 m thick and composed of clay sandstone with interbedded coal layers (Macquet et al., 2019).
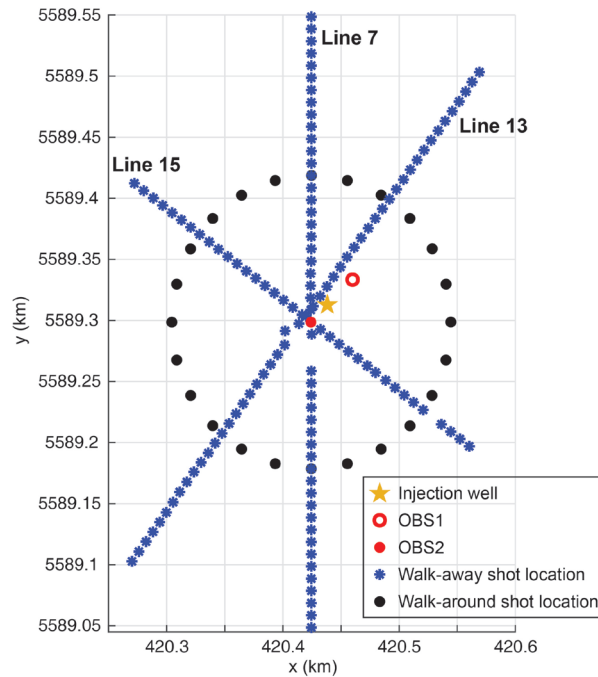

Figure 1: VSP layout map of the survey acquired in March 2021.

VSPs record both downgoing and upgoing seismic wavefields; therefore, upgoing reflections need to be isolated from DAS VSP data for impedance inversion. We separate downgoing and upgoing wavefields through the application of a 29-point median filter followed by a frequency-wavenumber (f-k) filter. Figure 2a shows the data from straight fiber in OBS2, in which downgoing P- or S-wave energy and upgoing P-wave energy are visible. After the median filter (Figure 2b) and f-k filter (Figure 2c), the upgoing P-wave reflections are clearly isolated and evident over the entire depth coverage of the fiber. Stacked seismic records can then be obtained from the isolated upgoing reflections after other standard VSP processing steps such as deconvolution, bandpass filtering, normal moveout correction and CDP stacking.
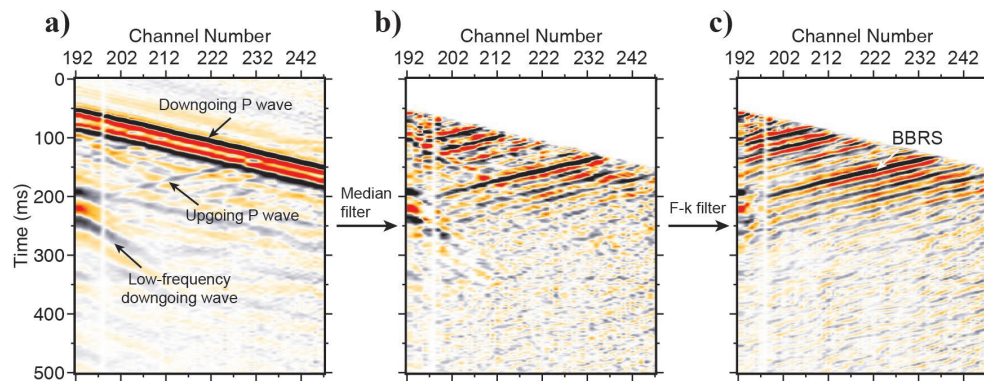

Figure 2: Wavefield separation: (a) raw DAS data from straight fiber in OBS2, and isolated upgoing wavefield after (b) median filter and then (c) f-k filter. BBRS reflection is indicated in plot (c).

DIFFERENT EI MEASURES

There are various EI definitions. From the linearization of Zoeppritz equation, the concept of EI was initially introduced by Connolly (1999):

$$EI = \rho V_P \left(\rho^{-4K\sin^2\theta} V_P^{\tan^2\theta} V_S^{-8K\sin^2\theta} \right), \tag{3}$$

where ρV_P is as in equation 1, V_S is the S-wave velocity and $K = (V_S/V_P)^2$. The K is assumed to be a constant, such as the average of V_S^2/V_P^2 over the interval of interest. Also, the dimensionality of EI in equation 3 varies with the incidence angle θ. To resolve the dimensionality issue, a normalized EI (NEI) was proposed by Whitcombe (2002):

$$NEI = \rho V_P \left[\left(\frac{\rho}{\rho_0} \right)^{-4K\sin^2\theta} \left(\frac{V_P}{V_{P,0}} \right)^{\tan^2\theta} \left(\frac{V_S}{V_{S,0}} \right)^{-8K\sin^2\theta} \right], \tag{4}$$

where $V_{P,0}$, $V_{S,0}$ and ρ_0 can be set equal to the corresponding properties of a formation such as the reservoir caprock. Nevertheless, this normalized EI is still with relative character and is from reflectivity integration along nonphysical paths of constant θ. To address these issues, another raypath EI (RI) is proposed, such as by Santos and Tygel (2004):

$$RI = \frac{\rho V_P}{\sqrt{1 - V_P^2 p^2}} \exp\left[-2(2+\gamma)V_S^2 p^2 \right], \tag{5}$$

where p is the ray parameter, and γ is a constant that relates ρ to V_S as $\rho = \rho_0 V_S^\gamma$. The RI is performed by integrating the reflectivity along the real path with ray parameter. In equation 5, there is no assumption of constant V_S/V_P ratio, but the constant γ is also difficulty to justify. In summary, all the above definitions of EI are derived from the integration of reflectivity and limited to different assumptions about the correlations of V_P, V_S and ρ. An exact expression of EI that truly represents the intrinsic physical property and accurately describe P- and S-wave propagations is highly desirable and described in the next subsection.

Exact EI matrix

This subsection briefly summarizes the EI matrix proposed by Morozov (2010). By considering a wavefield in the vicinity of a flat boundary that separates two isotropic elastic half-spaces, the strain for two components (x and z directions) of displacement is

$$\begin{pmatrix} e_{zz} \\ e_{zx} \\ e_{xx} \end{pmatrix} = \begin{pmatrix} \partial_z & 0 \\ \frac{1}{2}\partial_x & \frac{1}{2}\partial_z \\ 0 & \partial_x \end{pmatrix} \begin{pmatrix} u_z \\ u_x \end{pmatrix}. \tag{6}$$

Also, from Hooke's law, the stress-strain relation within an isotropic medium is

$$\sigma_{ij} = \lambda \delta_{ij} e_{kk} + 2\mu e_{ij},$$

(7)

where λ and μ are the Lamé constants, e_{kk} is the sum of diagonal elements of strain tensor, and δ_{ij} is the Kronecker symbol ($\delta_{ij} = 1$ for $i = j$, and $\delta_{ij} = 0$ for $i \neq j$). From equations 6 and 7, the traction on the flat boundary separating the two half-spaces is

$$\begin{pmatrix} \sigma_{zz} \\ \sigma_{zx} \end{pmatrix} = \begin{pmatrix} (\lambda + 2\mu)\partial_z & \lambda\partial_x \\ \mu\partial_x & \mu\partial_z \end{pmatrix} \begin{pmatrix} u_z \\ u_x \end{pmatrix}.$$

(8)

The operator $\tilde{\mathbf{Z}} = -\begin{pmatrix} (\lambda + 2\mu)\partial_z & \lambda\partial_x \\ \mu\partial_x & \mu\partial_z \end{pmatrix}$ relating the displacement to stress is defined as the impedance matrix, which would rigorously describe all cases of P/SV-wave propagation at arbitrary incidence angles (Morozov, 2010). Nevertheless, in acoustic, impedance is conventionally defined as the ratio of normal stress and velocity (Aki and Richards, 2002). By considering a plane wave with the displacement $u_{z,x} \propto \exp\left[i\left(k\cos\theta z + k\sin\theta x - \omega t\right)\right]$, where k is the wavenumber and θ is the incidence angle, the conventional impedance matrix can be defined as (Morozov, 2010)

$$\mathbf{Z} = \frac{i}{\omega}\tilde{\mathbf{Z}} = \frac{k}{\omega}\begin{pmatrix} (\lambda + 2\mu)\cos\theta & \lambda\sin\theta \\ \mu\sin\theta & \mu\cos\theta \end{pmatrix}.$$

(9)

For the situation of incident P-wave with wavenumber $k = \omega/V_P$, each component of impedance matrix $\mathbf{Z}$ in equation 9 becomes

$$\begin{aligned} Z_{zz,z} &= \rho V_P \cos\theta, \\ Z_{zz,x} &= \rho V_P \left(1 - 2V_S^2/V_P^2\right)\sin\theta, \\ Z_{xz,z} &= \rho V_P \left(V_S^2/V_P^2\right)\sin\theta, \\ Z_{xz,x} &= \rho V_P \left(V_S^2/V_P^2\right)\cos\theta, \end{aligned}$$

(10)

where the calculation reduces to the AI (ρV_P as in equation 1), and the V_S/V_P ratio from amplitude variation with offset (AVO) inversion. For the situation of P-wave at normal incidence, the $Z_{zz,z}$ in equations 10 would be the conventional AI (equation 1).

We then show and compare different impedance logs in the injection well from FRS CO_2 injection project. In Figure 3, the component $Z_{zz,z}$ (equations 10) is close to NEI (equation 4) and RI (equation 5) while the four components $Z_{zz,z}$, $Z_{zz,x}$, $Z_{xz,z}$, and $Z_{xz,x}$ show clear differences. All components of impedance matrix $\mathbf{Z}$ are required for achieving a complete and accurate description of reflection AVO effects.
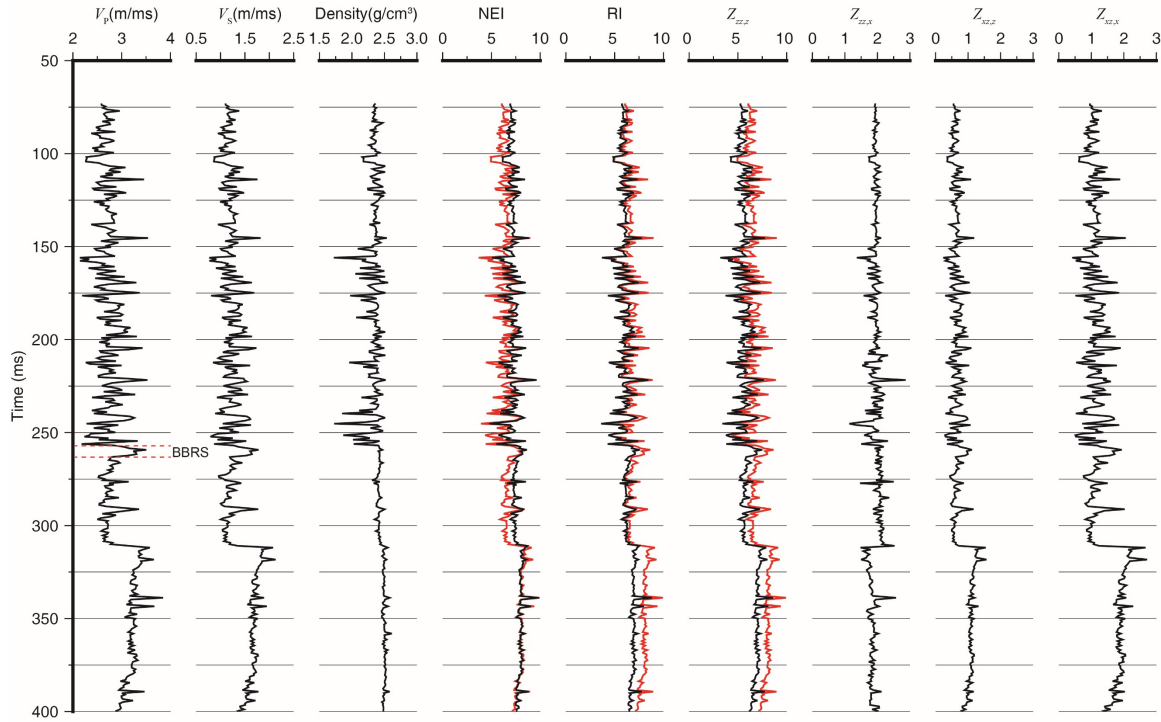
Figure 3: Velocity, density, NEI, RI and components of impedance matrix **Z** at 30° incidence angle in the injection well from the FRS CO_2 injection project. The AI log is shown in red in NEI, RI, and $Z_{zz,z}$ for comparison. The CO_2 injection zone BBRS is indicated.

RESULTS

This section describes the procedures for obtaining TL AI and EI variations. We first perform waveform calibration for TL VSP CDP stacks in order to obtain consistency of the amplitude and phases of the TL data and keeping the TL variations within the CO_2 injection zone. We use a well-log calibration inversion approach for getting the AI from baseline and calibrated monitor VSP CDP stacks, respectively. The EI and its TL variation are then evaluated from the inverted AI and V_S/V_P ratio.

Waveform calibration of TL data

The waveform calibration is performed to match each stacked monitor trace to the corresponding baseline trace by three operations of time shifting, amplitude correction, and spectral shaping. These three are similar to the operations of the widely used cross-equalization (Ross et al., 1996), but are applied locally by time-variant filtering using a series of overlapping Hann time windows. By matching monitor (u_{mon}) signal to baseline signal tapered within each window, the calibrated monitor signal (u_{cmon}) is obtained as

$$u_{cmon} = u_{mon} * f_{tim} * f_{amp} * f_{spec},$$ (11)

where "*" denotes the convolution operator, and linear filters f_{tim}, f_{amp}, and f_{spec} correspond to the three operations above, respectively. Each of the three filters in equation 11 is applied in frequency domain. The filter f_{tim} is expressed by phase shift $-2\pi i f \Delta t_1$, where f is the frequency and Δt_1 is the time shift. The filter f_{amp} is applied by

$A_{\mathrm{cmon}}(f) = A_{\mathrm{mon}}(f)e^{-\pi(f-f_0)t^*}$, where $A_{\mathrm{cmon}}(f)$ and $A_{\mathrm{mon}}(f)$ are the amplitude spectra. The amplitude correction is performed by a scaling factor s as $u_{\mathrm{cmon}}(f) = su_{\mathrm{mon}}(f)$.

Figure 4 shows the baseline (May 2017) VSP CDP stacks, and monitor (March 2021) VSP CDP stacks before and after the waveform calibration. The comparison shows that this approach is effective for matching the TL datasets. Figure 5 then shows two trace examples. The black wiggle lines (baseline and calibrated monitor traces) in each plot of Figure 5 become closer after calibration.
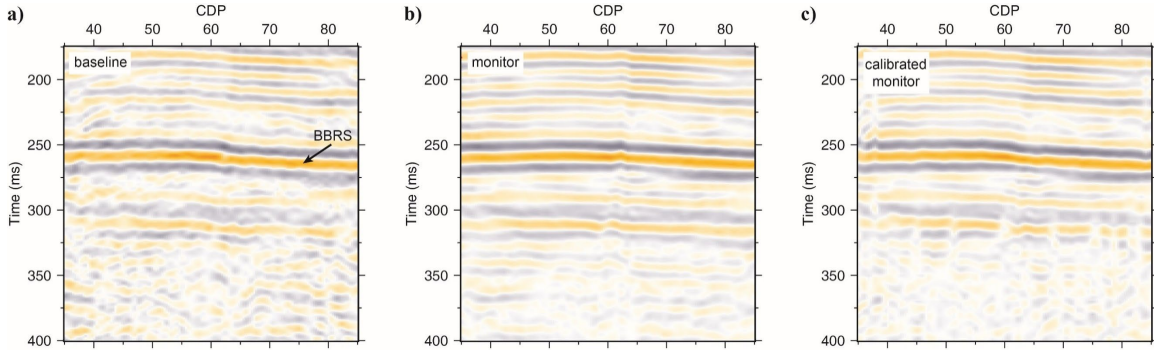
Figure 4: Cross sections of a) baseline, b) monitor and c) calibrated monitor VSP CDP stacks. The BBRS reflection is indicated.
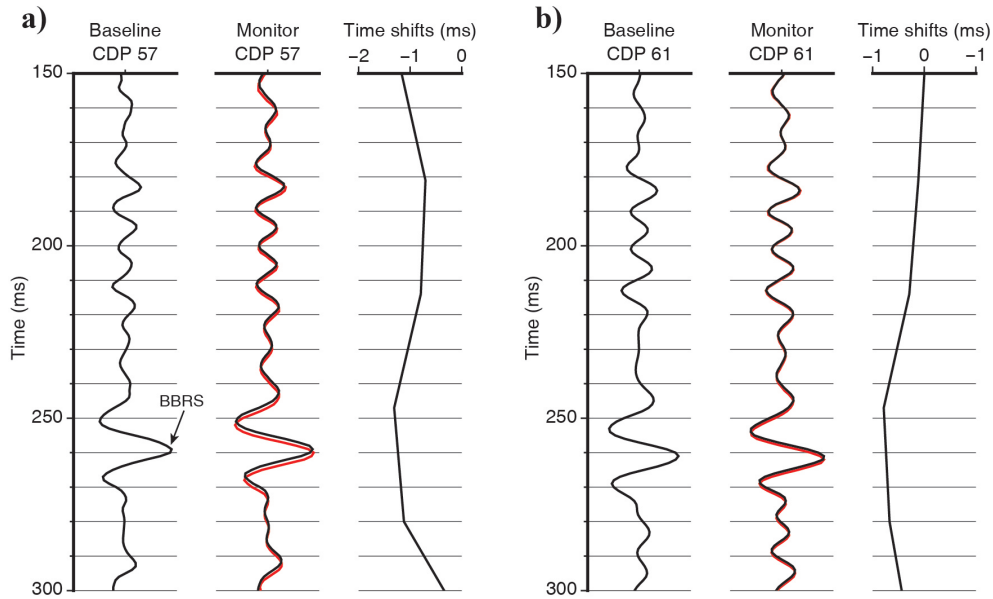

Figure 5: Application of waveform calibration to stacked monitor trace of CDP number (a) 57 and (b) 61 in Figure 4. The panels from left to right in plot (a) or (b) represent the baseline trace, the monitor trace before (red line) and after (black line) calibration, and the measured time shift Δt_1, respectively.

Impedance inversion and TL variations

We calculate the AI and its TL variations by using the well-log-based calibration method (Morozov and Ma, 2009). Although effectively performing impedance inversion from seismic reflection signals, this method does not require subjective selections of parameterization and regularization schemes and is implemented by time-variant matched filtering of seismic and well-log records. The method achieves a unique AI distribution satisfying the key requirements of a physically interpretable AI section: (1) the amplitude spectrum matches that of the well-log impedance near the imaging location, (2) below the seismic frequency band, the impedance also matches the one from well logs, and (3) at each imaging location, the spatial pattern of reflectivity matches that of the seismic volume (Wang and Morozov, 2020).

Figure 6 shows the inverted baseline and monitor AIs and their relative TL variations. The relative impedance variations (Z_{vari}) are derived as below:

$$Z_{vari} = \frac{Z_{cmon} - Z_{bas}}{Z_{bas}}, \tag{12}$$

where Z_{bas} and Z_{cmon} are the impedance from baseline and calibrated monitor stacks, respectively. In Figure 6c, the AI decrease of approximately 8% is around the OBS2 and injection well at the BBRS depth. This AI decrease is interpreted to be related to increased CO_2 saturation and/or pore pressure. The strongest decrease up to 10% is to the southwestern of OBS2, which could indicate the migration of the injected CO_2 changing from liquid phase at the injection well to gas phase at the leading edge of the plume.
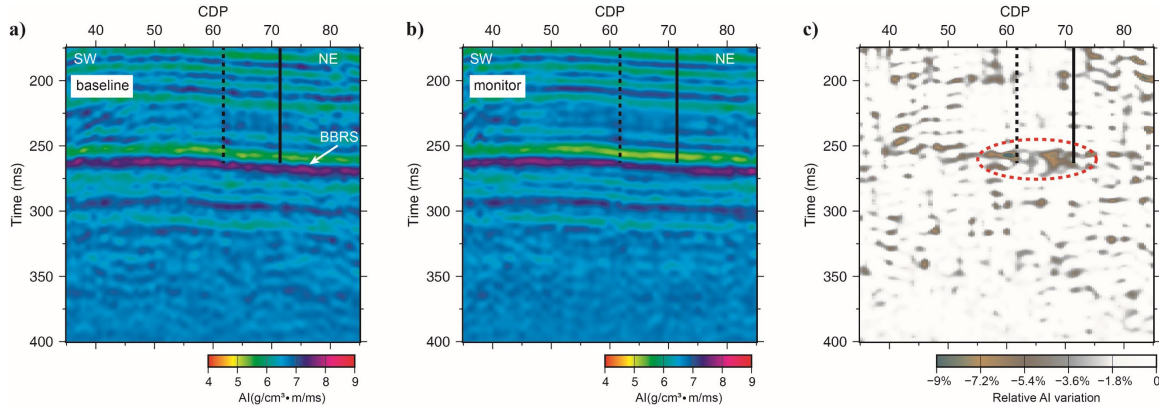

Figure 6: Cross sections of a) baseline AI, b) monitor AI and c) relative AI variations. Dashed and solid black lines indicate OBS2 and injection well, respectively.

Figure 7 then shows the $Z_{zz,z}$, $Z_{zz,x}$, $Z_{xz,z}$, and $Z_{xz,x}$ from AI and V_S/V_P ratio (equations 10) at a 30° incidence angle, and respective relative TL variations. The V_S/V_P ratio is currently from the well logs for this EI calculation, and we will derive the detailed 2D V_S/V_P ratio through AVO inversion. The TL variations of $Z_{zz,z}$ (Figure 7a) are similar to those of AI in Figure 6c while the decrease of $Z_{zz,x}$ (Figure 7b) is stronger. In addition, there are less variations of $Z_{xz,z}$, and $Z_{xz,x}$ (Figure 7c and 7d) than those of $Z_{zz,z}$ or AI within the BBRS injection zone due to the increase of V_S/V_P ratio at this depth.
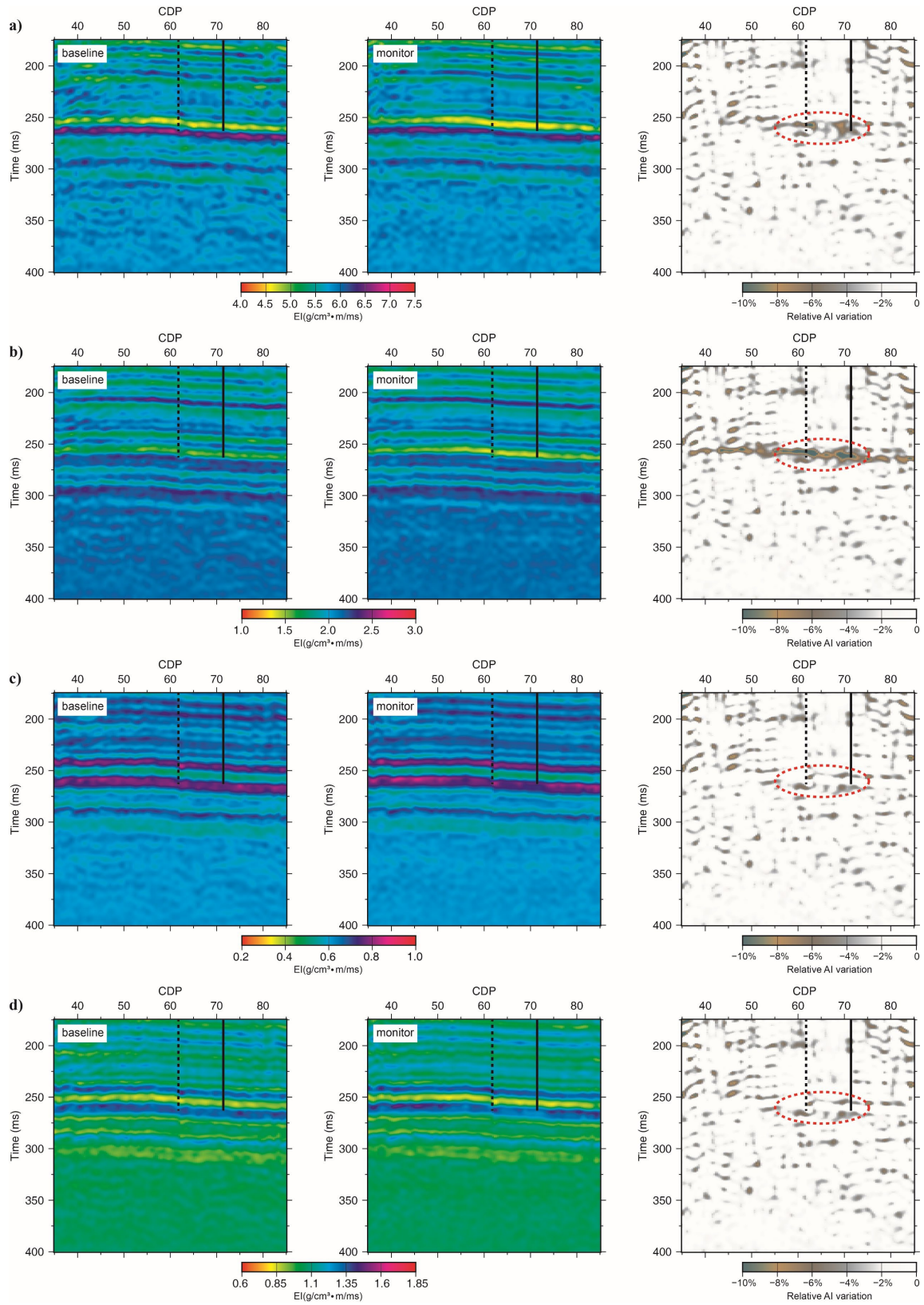
Figure 7: Cross sections of baseline and monitor EI and their TL variations of components a) *Zzz,z*, b) *Zzz,x*, c) *Zxz,z*, and d) *Zxz,x* of impedance matrix **Z** (equations 10) at 30° incidence angle.

CONCLUSIONS

For a CO_2 injection project at the CaMI FRS in Alberta, different DAS VSP surveys have been acquired for TL seismic monitoring. Stacked reflection records are obtained after upgoing wavefield separation and accurate waveform calibration is performed for matching the TL datasets. Impedances are inverted from baseline and calibrated monitor VSP CDP stacks respectively and impedance-variation images are then created. Reductions of the AI by approximately 8% are observed within the BBRS injection zone and correlated with injection well. This AI decrease is interpreted as caused by increases in CO_2 saturation and/or pore pressure. The exact expression of EI in a matrix form is measured, which can represent an intrinsic property of the medium and accurately describe wave propagations without any approximation. All components of this matrix EI are required for a complete description of AVO effects and different components show different levels of variations within the CO_2 injection zone. Such AI or EI can be advantageous to geologic CO_2-storage monitoring.

ACKNOWLEDGEMENTS

REFERENCES

Aki, K., and P. G. Richards, 2002, Quantitative seismology, 2nd ed.: University Science Books.

Connolly, P., 1999, Elastic impedance: The Leading Edge, 18, 438–452, doi: 10.1190/1.1438307.

Lindseth, R. O., 1979, Synthetic sonic logs — A process for stratigraphic interpretation: Geophysics, 44, 3–26, doi: 10.1190/1.1440922.

Lumley, D. E., 2001, Time-lapse seismic reservoir monitoring: Geophysics, 66, 50–53, doi: 10.1190/1.1444921.

Macquet, M., D. C. Lawton, A. Saeedfar, and K. G. Osadetz, 2019, A feasibility study for detection thresholds of CO_2 at shallow depths at the CaMI field research station, Newell County, Alberta, Canada: Petroleum Geoscience, 25, no. 4, 509–518, doi: 10.1144/petgeo2018-135.

Morozov, I. B., and J. Ma, 2009, Accurate poststack acoustic-impedance inversion by well-log calibration: Geophysics, 74, no. 5, R59–R67, doi: 10.1190/1.3170687.

Morozov, I. B., 2010, Exact elastic P/SV impedance: Geophysics, 75, no. 2, C7–C13, doi: 10.1190/1.3318268.

Santos, L.T., and M. Tygel, 2004, Impedance-type approximations of the P-P elastic reflection coefficient: Modeling and AVO inversion: Geophysics, 69, 592–598, doi: 0.1190/1.1707079.

Wang, Y., and I. B. Morozov, 2020, Time-lapse acoustic impedance variations after CO_2 injection in Weyburn Field: Geophysics, 85, no. 1, M1–M13, doi: 10.1190/geo2019-0221.1.

Whitcombe, D. N., 2002, Elastic impedance normalization: Geophysics, 67, 60–62, doi: 10.1190/1.1451331.

Ross, C. P., G. B. Cunningham, and D. P. Weber, 1996, Inside the cross-equalization black box: The Leading Edge, 15, 1233–1240, doi: 10.1190/1.1437231.